metals

MDPI

Article

Study on Flight Dynamics and Heat Transfer Solidification of Metal Droplets during Centrifugal Spray Deposition Forming Process

Peng Li [1,2], Shizhong Wei [2,*], Xianqing Lei [1,*], Lu Yang [2,3] and Bo Sun [1,2]

[1] School of Mechatronics Engineering, Henan University of Science and Technology, Luoyang 471003, China
[2] Joint Engineering Research Center for Abrasion Control and Molding of Metal Materials, Henan University of Science and Technology, Luoyang 471003, China
[3] School of Materials Science and Engineering, Henan University of Science and Technology, Luoyang 471003, China
* Correspondence: hnwsz@126.com (S.W.); ly-lxq@163.com (X.L.)

Abstract: Centrifugal spray deposition forming technology, which is used in the preparation process of near-net-forming billets, not only reduces the macroscopic segregation and refines the microstructures of billets but also has the characteristics of a rapid solidification structure. The trajectory, velocity, heat transfer and solidification of metal droplets granulated by the centrifugal force during flight will affect the shape, precision and microstructure of the billet. Therefore, it is necessary to study the dynamics and thermal history of droplets in flight. In this study, a single droplet is taken as the object. Considering the resistance of ambient gas, Newton's second law, classical nucleation theory, Newton's cooling law and the energy conservation equation were used to establish a dynamic model and heat transfer solidification model of liquid metal droplets during flight. The influence of the centrifugal disc speed on the diameter of granulated droplets was analyzed. The variation law of droplet flight trajectory and velocity was explored. The supercooling degree in metal droplet nucleation was quantified, and the influence of droplet diameter, superheat and other factors on heat transfer and solidification was revealed. The results show that the numerical calculation results are basically consistent with the previous research results. The trajectory of the droplet is parabolic during flight. The initial velocity of the droplet, the environmental gas resistance and the convective heat transfer coefficient are positively correlated with the rotating speed of the centrifugal disc; however, the droplet diameter is negatively correlated with the rotating speed of the centrifugal disc. The super cooling degree at the time of droplet nucleation and the flight time required for solidification are negatively correlated with the droplet diameter. Among them, the droplet diameter has a linear relationship with the solidification start time and a quadratic curve relationship with the solidification end time. The effect of superheat on the heat transfer and solidification of droplets is not obvious. The conclusions obtained can provide a theoretical basis for the determination of the preparation process parameters.

Keywords: centrifugal disc; rotation speed; granulation; droplet diameter; dynamics; heat transfer solidification; superheat

check for updates

Citation: Li, P.; Wei, S.; Lei, X.; Yang, L.; Sun, B. Study on Flight Dynamics and Heat Transfer Solidification of Metal Droplets during Centrifugal Spray Deposition Forming Process. *Metals* **2023**, *13*, 1446. https://doi.org/10.3390/met13081446

Academic Editors: Changming Fang and Masahiro Fukumoto

Received: 14 June 2023
Revised: 21 July 2023
Accepted: 9 August 2023
Published: 11 August 2023

Copyright: © 2023 by the authors. Licensee MDPI, Basel, Switzerland. This article is an open access article distributed under the terms and conditions of the Creative Commons Attribution (CC BY) license (https://creativecommons.org/licenses/by/4.0/).

1. Introduction

Centrifugal spray deposition technology uses the centrifugal force provided by a mechanical device to granulate liquid metal. The high-temperature droplets after granulation hit the moving substrate at high speed. The original kinetic energy and enthalpy of the droplets are used to tightly bond these droplets together. Due to the cooling effect of the substrate, a dense metal billet with rapid solidification structure characteristics is formed. Compared with traditional casting and powder metallurgy processes, this technology reduces the macrosegregation [1,2], eliminates multiple processing steps that are necessary

for powder metallurgy processing [3–5], refines the microstructure [6–8], expands the solid solubility [9–12] and has the advantage of near-net forming manufacturing [13,14]; therefore, it has attracted the attention of many scholars at home and abroad.

At present, most of the research on atomization deposition has mainly focused on the field of thermal spraying [15–18]. In [19], aluminum nitride–diamond composites were successfully prepared using plasma chemical vapor deposition technology. Different elastic modulus and hardness values were obtained by adjusting the deposition parameters, which proves that the material properties can be adjusted by changing the deposition parameters. In [20], the dynamic characteristics of an arc in a DC plasma torch were studied by using a three-dimensional transient equilibrium model. The variation in the dynamic parameters of the arc with time during deposition was proved, which provides a basis for the adjustment and determination of the process parameters. According to [21], the performance of plasma-sprayed coatings is closely related to the splashing and layered splashing of molten particles. The influence of viscosity and kinetic energy on particle flattening was analyzed and discussed. It was proved that the thickness of the flow boundary layer between flat droplets and the substrate has an important influence on droplet splashing, which lays a foundation for the subsequent control of droplet deposition. Ref. [22] used Fluent software to calculate the established model and obtained the energy required for the initial heating of the particles to their vaporization temperature under plasma conditions. This information, together with the energy lost due to the radiation from the particle surface during the evaporation process, provides a basis for quantifying the energy required for deposition. Ref. [23] used particle image velocimetry to study the direction and velocity of a plasma jet. The average impact velocity and impact angle of particles on the surface were determined by measuring the image velocity and segmentation size, and the motion parameters before deposition were quantified. In [24], the superhydrophobic ceramic coating was prepared by a vacuum plasma spray process for the solution precursor. The behavior and characteristics of droplets were analyzed and discussed using a theoretical formula during the deposition process. The relationship between the droplet diameter and deposition splash was established with the Stokes number, which provided a theoretical basis for determining the particle diameter. Based on the computational fluid dynamics and the numerical simulation of the direct-simulation Monte Carlo model, a two-step thermal plasma-assisted physical vapor deposition process was simulated in [25]. The effects of the process geometry and operating conditions on the airflow field and powder vaporization efficiency were predicted. The study provides a basis for the determination of deposition process parameters and the quantification of geometry size. In [26], the dynamics and thermal history of gas-detonation-sprayed Fe-40Al intermetallic powder particles were evaluated using Ansys Fluent CFD software and a self-developed algorithm, Ansys is a large general purpose finite element analysis (FEA) software developed by ANSYS, USA. Fluent is integrated in Ansys. The relationship between the dynamic parameters of the particles and time was obtained. The results obtained provide a theoretical explanation for the microstructure of the sedimentary layer.

Through the above studies, it can be seen that the experimental research is mainly focused on the microstructure of the deposited layer via SEM, XRD, etc. The theoretical research based on the previously described models mainly reflects the movement and heat transfer of the droplets. This is because the micron-sized and high-temperature droplets that occur in the spraying process are not convenient for experimental research. Since the spraying parameters are generally not changed during the deposition process, the temperature and velocity of the droplets before they have any impact on the substrate will not only affect the deposition efficiency but also the microstructure. It is very important to study the dynamics and heat transfer of droplets during flight during the forming process.

This paper will use Newton's second law, classical nucleation theory, Newton's cooling law and the energy conservation equation to establish relevant mathematical models. The flight trajectory, velocity, supercooling degree, heat transfer and solidification of the droplets

after granulation are numerically simulated by the model, which provides a theoretical basis for the development and research of the subsequent related experiments.

2. Model Establishment

2.1. Introduction of Physical Model

Figure 1 is a schematic diagram of centrifugal spray deposition forming for blank preparation. The basic process of forming is where the molten metal flows out from the crucible through the conduct pipe to the center of the high-speed, rotating, centrifugal disc. Under the action of inertial force and centrifugal force, the liquid metal spreads along the radial direction of the centrifugal disc and forms a liquid film on the centrifugal disc. When the surface tension of the liquid film is not enough to balance the centrifugal force required for its rotation, it will be released from the bondage caused by the surface tension and be transformed into droplets. The droplets exchange heat with the ambient gas during the flight and hit the substrate with a reciprocating motion at high speed. Then, the deposition layers are formed and, finally, a blank of a certain size is prepared. Since the centrifugal granulation of liquid metal is a complex process, it involves the granulation of liquid metal on the edge and the outside of the centrifugal disc, and the heat transfer and solidification of droplets on the outside of the centrifugal disc.

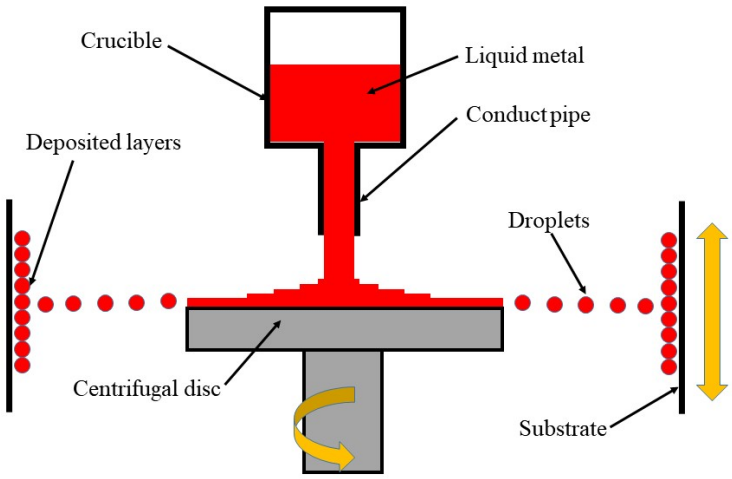

Figure 1. Schematic diagram of centrifugal spray deposition for blank preparation.

To simplify the calculations, the physical model makes the following assumptions:

(1) Due to the small diameter of the droplet, the droplet is regarded as a uniform sphere under surface tension.
(2) Due to the short flight time, as a rough estimate, the specific heat of the droplet at room temperature is taken as the research parameter.
(3) The relationship between the Weber number and droplet fragmentation is not considered. Droplets are granulated at the edge of the centrifugal disc.
(4) The velocity of the ambient gas is zero.
(5) The droplets do not collide with each other in flight.

2.2. Kinetic Model

In [27], when calculating the liquid film breakup and droplet formation models, it is assumed that the initial velocity is the same, and the model prediction results are in good agreement with the experimental results. Therefore, it is assumed that the droplets have the same initial velocity after granulation at the edge of the centrifugal disc; the speed diagram is shown in Figure 2. At this time, the initial velocity of the droplets is as follows:

$$u_0 = \sqrt{u_t^2 + u_r^2} \quad (1)$$

$$\vec{u}_t = k\omega D \tag{2}$$

$$u_r = \sqrt[3]{\frac{\rho_m k^2 \omega^2 Q^2}{6\pi D \mu_m}} \tag{3}$$

where $\vec{u}_t$ is the tangential velocity of the droplet at the edge of the centrifugal disc; u_r is the average radial velocity of the droplet at the edge of the centrifugal disc; ω is the rotational speed of the centrifugal disc; k is a constant equal to 0.1047198; D is the diameter of the centrifugal disc; ρ_m is the metal density; Q is the flow rate of the liquid metal; and μ_m is the viscosity of the liquid metal.

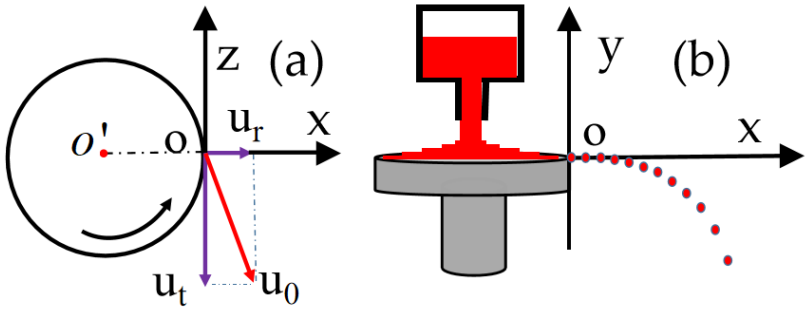

(a)Red and purple arrows represent the positive direction of velocity.

(b)The red circle represents the high temperature liquid metal particles.

Figure 2. Centrifugal spray deposition-forming speed diagram: (**a**) top view; (**b**) side view.

Liquid metal granulation can form droplets of different diameters; thus, d_m is the median mass diameter, which we used to characterize the dimensional characteristics of droplets.

By studying the relationship between the diameter of the atomized droplet and the rotational speed of the centrifugal disc, the diameter of the centrifugal disc and the volume flow rate of the liquid, it was found that the rotational speed of the centrifugal disc had the greatest influence on the droplet diameter, followed by the diameter of the centrifugal disc and, finally, the volume flow rate. The diameter of the droplet can be calculated using the following formula [28]:

$$d_m = 4.27 \times 10^6 \frac{1}{(k\omega)^{0.95}} \left(\frac{\gamma_m}{\rho_m}\right)^{0.42} \frac{Q^{0.12}}{D^{0.61}} \tag{4}$$

where d_m is the median mass diameter, the constant k is 0.1047918 and γ_m is the surface tension of the metal.

Metal droplets are mainly affected by three forces during flight: gravity, buoyancy and flight resistance. A schematic diagram of the force analysis is shown in Figure 3.

According to Newton's second law, the kinetic equation for the motion of metal droplets is

$$\vec{F}_G + \vec{F}_D + \vec{F}_L = m\frac{d\vec{u}_m}{dt} \tag{5}$$

$$m = \frac{\pi}{6} d_m^3 \rho_m \tag{6}$$

$$\vec{F}_G = \frac{1}{6}\pi\rho_m \vec{g} d_m^3 \tag{7}$$

$$\vec{F}_D = \frac{1}{8}\pi C_d \rho_g d_m^2 |u_m - u_g| \cdot (u_m - u_g) \tag{8}$$

$$\vec{F}_L = \frac{1}{6}\pi\rho_g \vec{g} d_m^3 \tag{9}$$

C_d is the resistance coefficient [29,30], which can be obtained by the following formula:

$$C_d = 0.28 + \frac{21}{\mathrm{Re}} + \frac{6}{\sqrt{\mathrm{Re}}} \tag{10}$$

$$\mathrm{Re} = \frac{\rho_g d_m |u_m - u_g|}{\mu_g} \tag{11}$$

where m is the mass of the droplet; ρ_g is the gas density; u_m is the velocity of the metal droplet; u_g is the velocity of the ambient gas; C_d is the drag coefficient; Re is the Reynolds number; μ_g is the viscosity of the gas; $\vec{F}_G$ is the gravity of the droplet, where the force direction in the vertical direction is positive; $\vec{F}_D$ is the droplet flight resistance, which is positive like the velocity direction; $\vec{F}_L$ is the buoyancy of the droplet, where the force direction in the vertical direction is positive; α is the angle between the velocity and horizontal direction; and t is the droplet flight time.

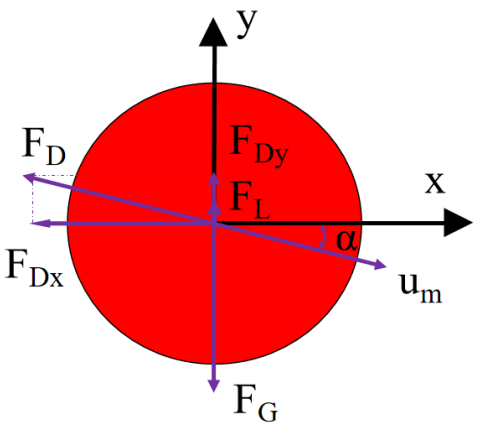

The red circle represents a high temperature spherical droplet.

The purple arrow represents the positive direction (force, velocity).

Figure 3. Force analysis of droplet.

Since α is relatively small, it is approximately zero; so, $F_G \gg F_{Dy}$. Ignoring the role of F_{Dy}, the acceleration of the metal droplet can be obtained from Equations (5)–(11).

$$\frac{d\vec{u}_m}{dt} = (-1 + \frac{\rho_g}{\rho_m})\vec{g} - \frac{3C_d\rho_g}{4d_m\rho_m}|u_m - u_g| \cdot (u_m - u_g) \tag{12}$$

As $\rho_m \gg \rho_g$ and, thus, $F_G \gg F_L$, by ignoring the effect of buoyancy F_L, the droplet acceleration can be simplified as

$$\frac{d\vec{u}_m}{dt} = -\vec{g} - \frac{3C_d\rho_g}{4d_m\rho_m}|u_m - u_g| \cdot (u_m - u_g) \tag{13}$$

Formula (13) is a vector differential equation that can be obtained by projecting it in the x and y directions.

$$\frac{du_{mx}}{dt} = -g_x - \frac{3C_d\rho_g}{4d_m\rho_m}|u_m - u_g| \cdot (u_{mx} - u_{gx}) \tag{14}$$

$$\frac{du_{my}}{dt} = -g_y - \frac{3C_d\rho_g}{4d_m\rho_m}\left|u_m - u_g\right| \cdot \left(u_{my} - u_{gy}\right) \tag{15}$$

$$\left|u_m - u_g\right| = \sqrt{\left(u_{mx} - u_{gx}\right)^2 + \left(u_{my} - u_{gy}\right)^2} \tag{16}$$

where u_{mx} is the velocity projection of the droplet in the x direction, u_{my} is the velocity projection of the droplet in the y direction, u_{gx} is the velocity projection of ambient gas in the x direction and u_{gy} is the velocity projection of the ambient gas in the y direction.

2.3. Heat Transfer Solidification Model

The metal droplets fly at a higher speed relative to the surrounding gas; thus, the droplets transfer heat to the surrounding gas and the mold wall via convective heat transfer and radiative heat transfer. Due to the droplet having a Bi < 0.1, and ignoring the temperature gradient along the diameter direction inside the metal droplet, the heat transfer process of the droplet satisfies the Newton cooling law. The convective heat transfer coefficient can be expressed as follows [31,32]:

$$h = \frac{K_g}{d_m}(2 + 0.6\mathrm{Re}^{0.5}\mathrm{Pr}^{0.33}) \tag{17}$$

$$\mathrm{Pr} = \frac{c_g\mu_g}{K_g} \tag{18}$$

where h is the convective heat transfer coefficient between the droplet and ambient gas, K_g is the thermal conductivity of the gas, Pr is the Prandtl number of the gas and c_g is the specific heat capacity of the gas.

The heat loss of the droplet during flight is compensated for by the enthalpy of the droplet. The change rate of the enthalpy of the metal droplet can be expressed by the relationship between the temperature of the metal droplet and the solid fraction during solidification. According to the conservation of energy, we can obtain the following formula:

$$\rho_m c_m \frac{dT}{dt} = \rho_m L \frac{df_s}{dt} - \frac{6h(T - T_g)}{d_m} - \frac{6\sigma\varepsilon(T^4 - {T_g}^4)}{d_m} \tag{19}$$

where c_m is the specific heat capacity of the metal; $\triangle T$ is the variation of metal droplets during flight; T is the temperature of the metal droplet; T_g is the gas temperature, which is the same as the ambient temperature; σ is the Stefan–Boltzmann constant; ε is the emissivity of the metal droplets; L is the latent heat of the melting metal; f_s is the solid fraction in the droplet; and t is the flight time.

The velocity of the droplet, the temperature difference between the droplet surface and the surrounding environment, and the emissivity of the surface and the wall surface are considered. It was found that radiation heat transfer plays a small role even under a large temperature difference; so, it was ignored. Therefore, during the flight of the metal droplets, the convective heat transfer on the surface of the droplets plays a leading role. The relationship between droplet temperature and time can be simplified with the following equation:

$$\frac{dT}{dt} = \frac{L}{c_m}\frac{df_s}{dt} - \frac{6h(T - T_g)}{d_m c_m \rho_m} \tag{20}$$

Most researchers believe that in order to accurately predict the temperature distribution of droplets, the supercooling and nucleation of droplets should be considered, and that the nucleation mode of droplets is mainly heterogeneous nucleation. From the classical nucleation theory, the nucleation rate can be found with Formula (21) [33].

$$I(T) = 10^{40}\exp\left(-\frac{16\pi T_L^2\gamma_{SL}^3 f(\theta)}{3k_B T\rho_m^2 L^2(T_L - T)^2}\right) \tag{21}$$

$$f(\theta) = \frac{1}{4}(2 - 3\cos\ \theta + \cos^3\ \theta) \tag{22}$$

where k_B is the Boltzmann constant, γ_{SL} is the solid–liquid interface energy, T_L is the liquids temperature of the metal and θ is the wetting angle.

According to the study of EON-SIK [30,33], the contact angle factor can be expressed as

$$f(\theta) = -5.025 \times 10^{-3} + 1.005 \times 10^{-6} \cdot d_m^{-1} \tag{23}$$

It is assumed that in a droplet with a volume of V_d, the formation of a nucleus represents the beginning of the nucleation process, which can be expressed by the following formula:

$$V_d \int_{T_N}^{T_L} \frac{I(T)}{\dot{T}} dT = 1 \tag{24}$$

where $\dot{T}$ is the droplet cooling rate, T_N is the nucleation temperature and V_d is droplet volume.

$I(T)$ is essentially zero, except for in a very narrow temperature range near T_N. Therefore, by introducing the correlation coefficient $\alpha(0 < \alpha < 1)$, it can be assumed that the narrow temperature range is represented by $\alpha(T_L - T_N)$, where $I(T)$ equals $I(T_N)$. So, the critical condition becomes

$$\frac{\alpha(T_L - T_N)\ V_d I(T_N)}{\dot{T}} = 1 \tag{25}$$

Considering that the formed product is a multi-element and multi-metal alloy billet, the droplet will undergo five stages during flight, including liquid-phase cooling, nucleation and recalescence, segregation solidification, eutectic transformation and solid-phase cooling.

(1) Liquid-phase cooling

During liquid-phase cooling, the droplet's temperature changes from the initial temperature to the nucleation temperature (T_N).

The droplet transfers heat to the surrounding environment, causing its own temperature to decrease, and the droplet as a whole is a liquid—that is, the solid-phase fraction of the droplet is zero.

The expression for the cooling process is

$$\frac{dT}{dt} = -\frac{6h(T - T_g)}{d_m \rho_m c_m} \tag{26}$$

(2) Nucleation and recalescence

Once the liquid temperature reaches the nucleation temperature, the recalescence process begins to germinate.

Because recalescence is driven by supercooling, the latent heat release rate decreases with the increase in droplet temperature. Once the latent heat release rate is equal to the heat absorption rate from the droplet surface, the latent heat release rate decreases with the increase in droplet temperature. The recalescence process ends and the heat balance equation is

$$\frac{L}{c_m}\frac{df_s}{dt} = \frac{6h(T_R - T_g)}{d_m c_m \rho_m} \tag{27}$$

where T_R is the recalescence temperature.

In addition, studies have shown that the growth rate of the solid phase in the undercooled melt can be estimated as follows:

$$\frac{df_s}{dt} = \frac{k_i(T_L - T)}{d_m} \tag{28}$$

where k_i is the interfacial adhesion coefficient.

The maximum solid fraction at the end of recalescence can be estimated by

$$f_R = \frac{(T_L - T_N)c_m}{L} \tag{29}$$

where f_R is the maximum solid fraction at the end of recalescence.

(3) Segregation solidification

After the recalescence stage, the next process of solidification of the remaining liquid in the droplet is carried out via segregation solidification. The heat balance equation during segregation solidification is

$$\frac{dT}{dt} = -\frac{6h(T - T_g)}{c_m \rho_m d_m} \cdot \left(1 - \frac{L}{c_m}\frac{df_s}{dT}\right)^{-1} \tag{30}$$

The solid fraction at this stage can be obtained by the modified Scheil equation [34].

$$f_s = 1 - (1 - f_R)\left(\frac{T_M - T}{T_M - T_R}\right)^{\frac{1}{k_0 - 1}} \tag{31}$$

$$\frac{df_s}{dT} = \frac{(1 - f_R)}{(k_0 - 1)(T_M - T_R)} \cdot \left(\frac{T_M - T_R}{T_M - T}\right)^{\frac{k_0 - 2}{k_0 - 1}} \tag{32}$$

$$\frac{df_s}{dt} = \frac{df_s}{dT} \cdot \frac{dT}{dt} \tag{33}$$

where T_M is the melting point of the pure alloy solvent and k_0 is the partition ratio.

(4) Eutectic transformation

When the segregation solidification is carried out to the point that it reaches the eutectic transition temperature, the residual liquid phase in the droplet undergoes eutectic transformation [35]. During the eutectic transformation, the droplet temperature is maintained at the eutectic temperature until the curing is completed. The solid fraction in the process can be expressed as

$$\frac{df_s}{dt} = \frac{6h(T_E - T_g)}{\rho_m d_m L} \tag{34}$$

where T_E is the eutectic temperature.

(5) Solid-phase cooling

When $f_s = 1$, the segregation solidification is considered to be over. In the solid-phase cooling stage, the droplet reduces the temperature through convective heat transfer. The heat balance equation at this stage can be described by Formula (26) from the liquid-phase cooling stage.

3. Numerical Experiment

The droplet diameter had an important influence on the forming blank, and the droplet diameter was greatly affected by the rotational speed of the centrifugal plate. Therefore, the numerical experiment of the rotational speed of the centrifugal plate on the droplet dynamics and heat transfer is carried out. The diameter of the centrifugal disc is 50 mm, the liquid metal flow rate is 4.86×10^{-6} m^3/s and nitrogen is used as the ambient gas, of which physical properties are shown in Table 1.

Table 1. Physical properties of ambient gas (N_2).

ρ_g/(kg/m^3)	μ_g/(Pa · s)	K_g/(W/m · K)	c_g/(J/kg · K)	T_g/(K)
1.1616	1.873×10^{-5}	0.0258	1043.21	313.15

Considering the price, melting point and social demand of the experimental materials, we used a low-melting point A390 aluminum alloy as the centrifugal spray forming material for calculation. The density and specific heat parameters were calculated using the values at room temperature. The physical properties of A390 aluminum alloy are shown in Table 2.

Table 2. Physical properties of A390.

$\rho_m/(\mathrm{kg/m^3})$	$\mu_m/(\mathrm{Pa \cdot s})$	$T_M/(\mathrm{K})$	$T_L/(\mathrm{K})$	$T_E/(\mathrm{K})$	α
2633	0.002	934	913	850	0.01
$\gamma_m/(\mathrm{N/m})$	$\gamma_{SL}/(\mathrm{J/m^2})$	$c_m/(\mathrm{J/kg \cdot K})$	$L/(\mathrm{J/kg})$	K_0	$k_i(\mathrm{m \cdot s^{-1} \cdot K^{-1}})$
0.768	0.2298	865.8	5.456×10^5	0.14	0.01

Formulas (1)–(34) describe the basic laws of droplet motion, temperature, solid fraction and cooling rate after centrifugal granulation. In general, the above equations are first-order nonlinear ordinary differential equations. Based on the Matlab platform, MATLAB is a commercial mathematics software produced by MathWorks Company in the United States. The version used in this article is MATLAB 9.11, the fourth-order Runge–Kutta method with a high calculation accuracy was used to solve the problem. In the calculation, the relevant data were the first inputs, where Formula (1) was the initial condition and Formula (16) was the constraint condition. Then, the droplet size was calculated; finally, the droplet velocity, solid fraction and temperature were calculated.

4. Results and Discussion

4.1. The Relationship between Rotational Speed and Droplet Diameter

The relationship between the rotation speed of the centrifugal disc and the droplet diameter can be obtained from Formula (4). As shown in Figure 4, the droplet diameter decreases with the increase in the rotation speed of the centrifugal disc because the greater the rotation speed, the greater the centrifugal force on the liquid film. The variation trend in the droplet diameter is consistent with the research findings in [36,37]. When the rotational speed is less than 15,000 r/min, the droplet diameter decreases significantly with the increase in rotational speed. The droplet diameter corresponding to the initial position of 4000 r/min is connected with the droplet diameter corresponding to the initial position of 15,000 r/min. The average slope K_1 is −42, indicating that the droplet diameter decreases by 42 μm with the increase in the rotational speed of 1000 r. The droplet is greatly affected by the rotational speed in this range, and the droplet diameter in this range is 184–647 μm. When the rotation speed is greater than 15,000 r/min, the droplet diameter does not change significantly with the increase in the rotation speed. The droplet diameter corresponding to 15,000 r/min is connected to the droplet diameter corresponding to 35,000 r/min, and the average slope is −5, indicating that the droplet diameter decreases by 5 um when the rotation speed increases by 1000 r. The droplet diameter in this interval is less affected by the rotation speed. The droplet diameter is 82–184 μm, and the droplet diameter after granulation is relatively stable. When it is greater than 25,000 r/min, the effect of increasing the rotation speed on the droplet diameter decreases. In the range of 15,000–25,000 r/min, we selected five different diameters of droplets (184 μm, 155 μm, 140 μm, 123 μm and 113 μm) for analysis and calculation.

4.2. Droplet Flight Trajectory

The droplet flight trajectory can be obtained from Formulas (14) and (15). As shown in Figure 5, the shape of the droplet trajectory is a parabola and the trajectory is consistent with the study in [38]. When the vertical displacement is constant, the horizontal displacement increases with the decrease in droplet diameter. It can be seen from Formulas (1)–(4) that the larger the droplet diameter, the smaller the initial velocity of the droplet. At the same time, the figure also shows that the vertical displacement and the horizontal displacement are quite different. In the case of a vertical displacement of 10 mm, the droplet diameter is

from 184 to 113 μm, and the ratio of vertical displacement to horizontal displacement is 0.0071, 0.0063, 0.006, 0.0057 and 0.0056. It can be seen that the smaller the droplet diameter, the smaller the ratio, and the vertical displacement accounts for almost none of the total displacement. Therefore, the vertical displacement of the droplet can be ignored in regard to the motion of the substrate, and the horizontal displacement can be approximated as the total displacement in the follow-up study.

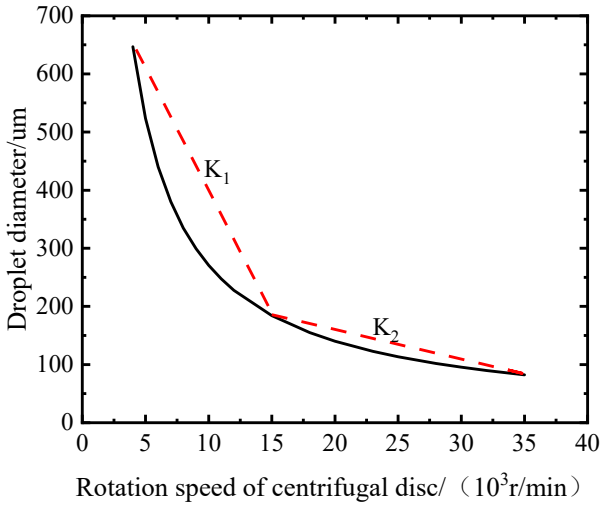

Figure 4. Relationship between centrifugal disc speed and droplet diameter.

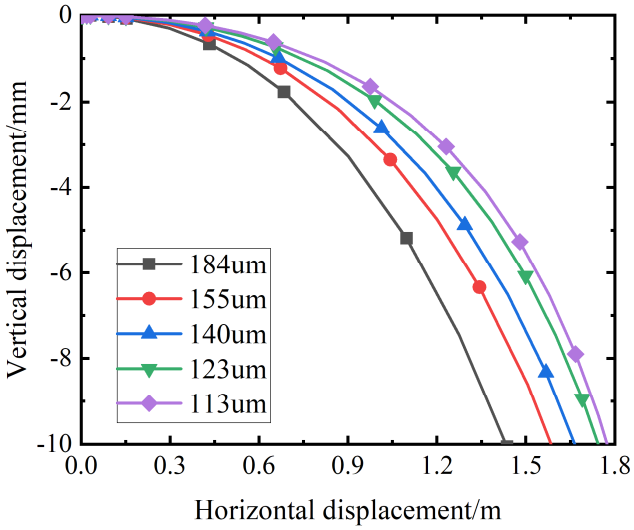

Figure 5. Droplet flight trajectory.

4.3. The Relationship between Droplet Flight Time and Motion Parameters

The relationship between the droplet flight time and the horizontal displacement and velocity can be obtained from Formulas (14) and (15), as shown in Figure 6. At the same time, the droplet flight displacement increases with the decrease in the droplet diameter. It can be seen from Formulas (1)–(4) that the smaller the droplet diameter, the greater the initial speed. The larger the initial velocity of the droplet, the more obvious the velocity changes with time during flight. From Formula (9), it can be seen that the droplets with a large initial velocity are subjected to a large amount of environmental gas resistance. At the same time, from Formula (6), it can be seen that the smaller the droplet size means the smaller the inertia, and it is easier to change its speed; thus, the droplet velocity changes significantly at a high speed. The change in the droplet flight velocity and displacement is consistent with the literature [38,39].

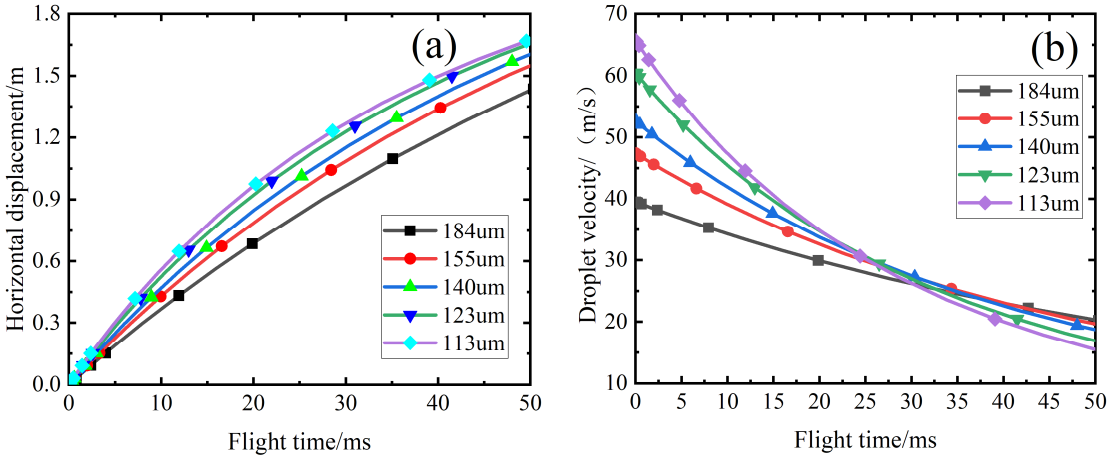

Figure 6. The relationship between droplet flight time and motion parameters: (**a**) horizontal displacement; (**b**) droplet velocity.

4.4. Relationship between Droplet Flight Time and Convective Heat Transfer Coefficient

The relationship between droplet flight time and the convective heat transfer coefficient can be obtained from Formula (17), as shown in Figure 7. The convective heat transfer coefficient decreases with the increase in flight time, and the initial value increases with the increase in droplet diameter. Because Formula (17) contains Formulas (4) and (11), it can be seen that the convective heat transfer coefficient is negatively correlated with the droplet diameter and positively correlated with the velocity—that is, the convective heat transfer coefficient increases with the smaller droplet diameter and increases with the increase in velocity. During flight, the droplet diameter remains unchanged, and the velocity decreases with the increase in the distance, which reduces the convective heat transfer coefficient.

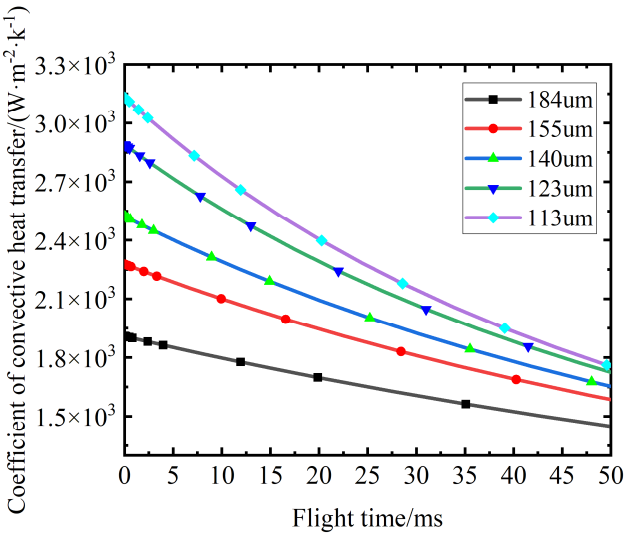

Figure 7. The convective heat transfer coefficients of different droplet diameters vary with time.

4.5. The Relationship between Flight Time and Heat Transfer Solidification

From Formulas (16)–(34), the relationship between the droplet flight time and the droplet temperature and solid fraction can be obtained. Figure 8 shows the relationship between droplet temperature, solid fraction and flight time at different rotational speeds when the superheat of the liquid alloy is 50 K—that is, the initial temperature is 963 K. It can be clearly seen that the droplets undergo five different stages: liquid-phase cooling, nucleation and recalescence, segregation solidification, eutectic solidification and solid-state cooling. In Figure 8a, it can be seen that the solidification temperatures corresponding to

the droplet diameter from 184 to 113 μm are 905 K, 899 K, 896 K, 892 K and 890 K. The solidification temperature decreases with the decrease in the droplet diameter, which means that the supercooling degree of the droplet is also greater. The droplet releases the latent heat caused by solidification in the nucleation and recalescence stages, and the temperature rises sharply to around 1 K below the liquidus temperature (913 K). The temperature in the segregation solidification stage decreases rapidly to the eutectic temperature. The initial temperature of eutectic solidification is 850 K, which has a slight downward trend with time but the downward trend is not obvious. When the eutectic solidification is completed, the droplet is further cooled. In Figure 8b, it can be seen that the solid fraction is zero at the beginning of the period of time, indicating that the droplet has not yet started to nucleate and is in the liquid-phase cooling stage. After a period of time, the solid fraction increases rapidly with a steep slope, indicating that the solidification has entered the nucleation and recalescence period. At this stage, the solid fraction of the droplet increases with the increase in the rotational speed. It can be seen from Formula (1) that the higher the rotational speed is, the greater the initial speed is. It can be seen from Formula (4) that the higher the rotational speed is, the smaller the droplet diameter is. High rotational speed and small-diameter droplets can lead to a higher convective heat transfer coefficient and, thus, to higher subcooling. The maximum solid fraction during this period was 0.01127, 0.0222, 0.0270, 0.0333 and 0.0365. With the increase in the solid fraction, the solidification enters the stage of segregation solidification. Finally, the growth rate of the solid fraction increases again, and the solidification enters the eutectic solidification stage until the solid fraction is 1. The results show that the variation trend in the temperature and solid fraction is consistent with that in the literature [40].

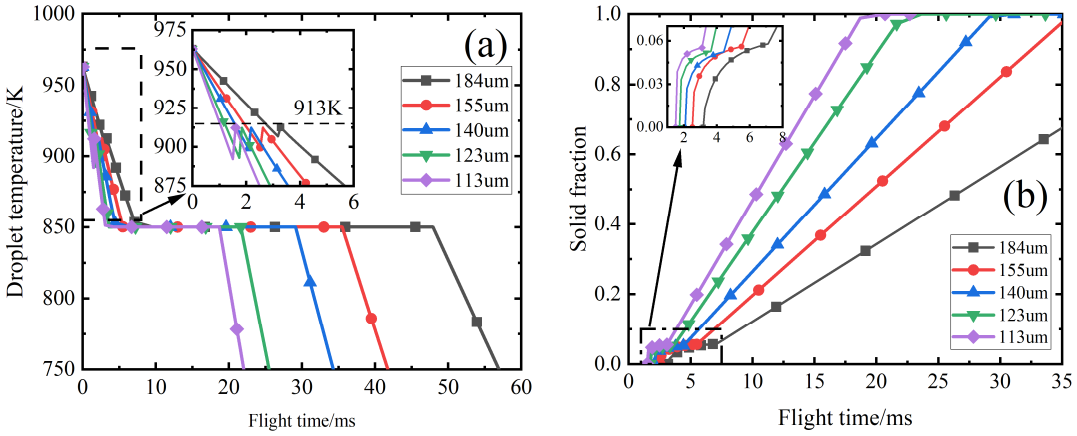

Figure 8. The relationship between flight time and heat transfer solidification: (**a**) droplet temperature; (**b**) solid fraction.

4.6. The Relationship between Droplet Solidification and Flight Time at Different Speeds

Figure 9 shows the relationship between the solidification of droplets and the flight time at different speeds. It can be seen from the diagram that with the increase in the rotational speed, the time required for the droplet to solidify from the beginning of solidification to complete solidification decreases from 44.74 ms to 17.2 ms. With the increase in rotational speed, the time required to start solidification gradually becomes shorter and the trend is linear. The fitting curve is $t_1 = -0.166\omega^2 + 5.57$. This formula can be used to predict whether the droplets begin to solidify at different speeds. Complete solidification decreases with the increase in rotational speed, and the trend is a quadratic curve. The fitting curve equation is $t_2 = 0.169\omega^2 - 9.66\omega + 154.79$. This formula can be used to predict whether the droplets are completely solidified at different rotational speeds.

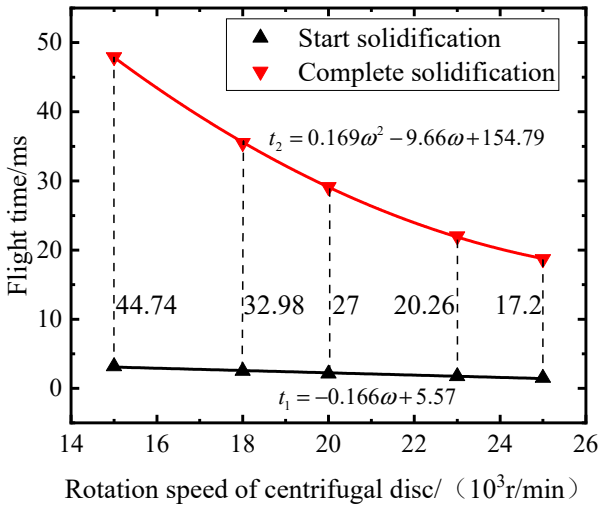

Figure 9. The relationship between droplet solidification and flight time at different speeds.

4.7. Effect of Superheat on Heat Transfer Solidification

Figure 10 shows the relationship between the flight time, superheat and solid fraction. When the superheat is 50 K, 100 K and 150 K, the initial temperature is 963 K, 1013 K and 1063 K, respectively. The time required for the droplets to cool to the nucleation temperature increases with the increase in the superheat. This is highly consistent with the findings presented in the literature [39]. The maximum solid fraction remains unchanged at 0.06 at the end of segregation solidification. The time required for eutectic solidification and solid-phase cooling also increases with the increase in the superheat. In the case of the same rotational speed, Formulas (1), (4) and (17) show that the initial velocity, diameter and flow heat transfer coefficient of the droplet are the same. The higher the temperature, the longer the cooling time; because the nucleation temperature is constant, it can be seen from Formula (29) that the maximum solid fraction during nucleation and recalescence is constant.

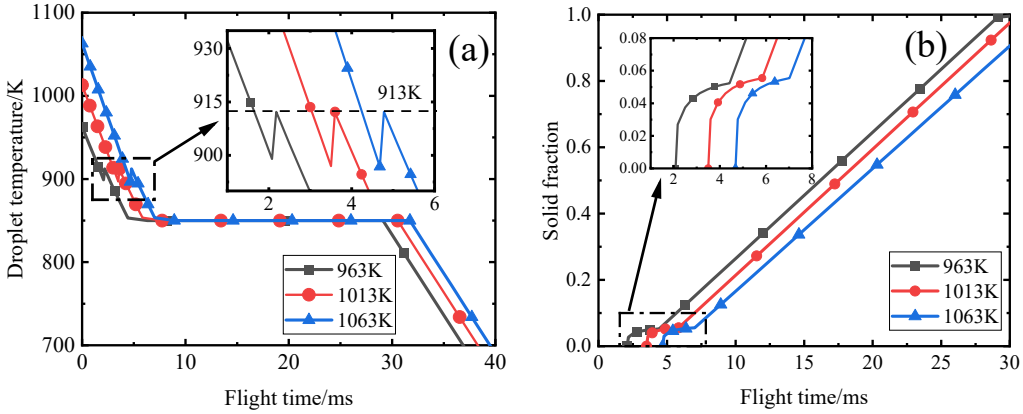

Figure 10. Effect of superheat on heat transfer solidification: (**a**) droplet temperature; (**b**) solid fraction.

4.8. The Relationship between Droplet Solidification and Flight Time under Different Superheats

Figure 11 shows the relationship between the start and end of droplet solidification and flight time at different temperatures. It can be seen that with the increase in the droplet temperature, the time from initial solidification to complete solidification increases from 27 ms to 28.04 ms. With the increase in temperature, the time when the droplets begin to solidify becomes longer and the trend is linear. The fitting curve equation is $t_3 = 0.036T - 5.67$. This equation can be used to predict whether the droplets begin to solidify at different temperatures. With the increase in temperature, the time until the complete solidification of the droplets becomes longer and the trend is linear. The fitting

curve equation is $t_4 = 0.026T - 22.5$. We can use this formula to predict whether the droplets are completely solidified at different temperatures.

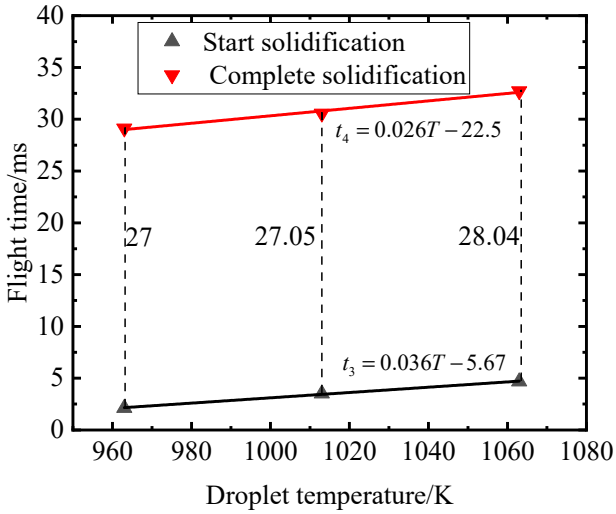

Figure 11. Relationship between solidification and flight time of droplets at different temperatures.

5. Conclusions

Under the condition that the flow rate of molten metal is constant, this study analyzed the trajectory of droplets and the relationship between the flight time and the speed, displacement, convective heat transfer coefficient, superheat, temperature and solid-phase ratio by combining Newton's second law, classical nucleation theory, Newton's law of cooling and the energy conservation equation. The following conclusions can be drawn:

1. The droplet diameter decreases with an increase in rotational speed. When the rotational speed is lower than a certain value, the droplet diameter is greatly affected by the rotational speed. When the rotational speed is higher than this value, the influence of rotational speed on the droplet diameter is weakened.
2. The flight trajectory of the droplet is parabolic; the flight displacement, initial velocity, ambient gas resistance and convective heat transfer coefficient increase with an increase in speed, and the vertical displacement of the droplet is not influenced by the movement of the substrate during the forming process.
3. In the forming process, the superheat has no obvious effect on the cooling and solidification process of the droplet, which is mainly affected by the speed of the centrifugal disc, and the time required for cooling and solidification decreases with the increase in speed.
4. Under the same superheat, the speed of the centrifugal disc is negatively correlated with the time required for droplet solidification, where the droplet starts to solidify in a linear relationship with the speed, and the time required for complete solidification is a quadratic function of the speed.
5. In the case of the same centrifugal disc speed, the superheat is positively correlated with the time required for the droplet to solidify, where the time required for the droplet to start solidifying and complete solidification is linear with the temperature.

Author Contributions: Conceptualization, methodology, software, validation and writing—original draft preparation, P.L.; formal analysis, funding acquisition and writing—review and editing, S.W.; supervision, writing—review and editing, X.L.; software, and resources, L.Y.; methodology and resources, B.S. All authors have read and agreed to the published version of the manuscript.

Funding: This work was financially supported by the National Key R&D Program of China (2020YFB2008400).

Institutional Review Board Statement: Not applicable.

Informed Consent Statement: Not applicable.

Data Availability Statement: Not applicable.

Conflicts of Interest: The authors declare no conflict of interest.

Nomenclature

u_0	initial velocity of the droplet (m/s)
u_t	tangential velocity of the droplet (m/s)
u_r	average radial velocity of droplets (m/s)
ω	rotation speed of the centrifugal disc (r/min)
D	diameter of the centrifugal disc (m)
ρ_m	metal density (kg/m^3)
Q	flow rate of the liquid metal (m^3/s)
μ_m	viscosity of the liquid metal (Pa·s)
d_m	diameter of the droplet (μm)
γ_m	surface tension of the metal (N/m)
F_G	gravity of the droplet (N)
F_D	resistance of the droplets (N)
m	mass of the droplets (kg)
ρ_g	gas density (kg/m^3)
C_d	drag coefficient (-)
u_m	velocity of the droplet (m·s^{-1})
u_{mx}	velocity projection of droplet in the x direction (m·s^{-1})
u_{my}	velocity projection of the droplet in the y direction (m·s^{-1})
u_g	velocity of the ambient gas (m·s^{-1})
u_{gx}	velocity projection of the ambient gas in the x direction (m·s^{-1})
u_{gy}	velocity projection of the ambient gas in the y direction (m·s^{-1})
h	convective heat transfer coefficient (W·m^{-2}·K^{-1})
K_g	thermal conductivity of gas (W·m^{-1}·K^{-1})
c_m	specific heat capacity of the metal (J·kg^{-1}·K^{-1})
c_g	specific heat capacity of the gas (J·kg^{-1}·K^{-1})
α	angle between the velocity and horizontal direction (°)
T	temperature of the metal droplet (K)
T_g	temperature of the ambient gas (K)
σ	Stefan–Boltzmann constant (W·m^{-2}·K^{-4})
L	latent heat of metal melting (J·kg^{-1})
γ_{SL}	solid–liquid interface energy (J·m^{-2})
T_L	liquidus temperature of the metal (K)
θ	wetting angle (°)
$\dot{T}$	droplet cooling rate (K·s^{-1})
T_N	nucleation temperature (K)
V_d	droplet volume (m^3)
T_R	recalescence temperature (K)
T_M	melting point of the pure alloy solvent (K)
T_E	eutectic temperature (K)
k_i	interfacial adhesion coefficient (m·s^{-1}·K^{-1})
k	constant value (-)
Re	Reynolds number (-)
k_0	melting point of the pure alloy solvent (-)
Pr	Prandtl number (-)
f_R	maximum solid fraction (-)
α	correlation coefficient (-)
f_s	solid fraction (-)
k_B	Boltzmann constant (-)
ε	emissivity of metal droplets (-)

References

1. Cui, J.; Li, B.; Liu, Z.; Qi, F.; Zhang, B.; Zhang, J. Numerical Investigation of Segregation Evolution during the Vacuum Arc Remelting Process of Ni-Based Superalloy Ingots. *Metals* **2021**, *11*, 2046. [CrossRef]
2. Li, C.; Liu, F.; Yu, F.; Qiao, H.; Zheng, D.; Le, Q. The growth mechanism and morphology evolution of primary Si during slow cooling solidification of high purity Al–15Si alloy with Cr additions. *J. Mater. Res. Technol.* **2023**, *23*, 1204–1213.
3. Kováčik, J.; Manonukul, A. New Insights of Powder Metallurgy: Microstructure, Durability and Properties. *Materials* **2023**, *16*, 2307. [PubMed]
4. Torralba, J.M. Powder Metallurgy: A New Open Section in Metals. *Metals* **2021**, *11*, 1519.
5. Ke, B.R.; Sun, Y.C.; Zhang, Y.; Wang, W.R.; Wang, W.M.; Ma, P.Y.; Ji, W.; Fu, Z.Y. Powder metallurgy of high-entropy alloys and related composites: A short review. *Int. J. Miner. Metall. Mater.* **2021**, *28*, 931–943.
6. Zhang, R.; Wang, S.; Lu, W.; Sun, F.; Huang, L.; Bolzoni, L.; Geng, L.; Yang, F. Enhancing microstructure refinement and strengthening efficiency of TiBw/near α-Ti composites by combining solid-solution treatment with hot processing. *Compos. Part B Eng.* **2023**, *257*, 110696.
7. Fan, Z.; Gao, F. Grain Initiation and Grain Refinement: An Overview. *Metals* **2022**, *12*, 1728.
8. Ma, R.; Zhang, X. Refining the microstructure to strengthen casting titanium alloy by electric pulse. *Mater. Sci. Eng. A* **2022**, *849*, 143519.
9. Yakovtseva, O.A.; Emelina, N.B.; Mochugovskiy, A.G.; Tabachkova, N.Y.; Prosviryakov, A.S.; Mikhaylovskaya, A.V. Influence of Pre-Milling on the Mn Solid Solubility in the Al-Mn-Cu Alloy during Mechanical Alloying. *Metals* **2023**, *13*, 756.
10. Chen, H.; Morita, K. Solid solubility and site preference of Ti in 3C-SiC. *Acta Mater.* **2021**, *212*, 116927.
11. Zuo, D.D.; Chang, J.; Liu, W.; Wang, H.P. Solid solubility extension and nano-mechanical properties of rapidly solidified Fe-Zr eutectic alloys under free fall condition. *J. Alloys Compd.* **2022**, *896*, 162928.
12. Mao, F.; Zhang, P.; Wei, S.; Chen, C.; Zhang, G.; Xiong, M.; Wang, T.; Guo, J.; Wang, C. Interface Microstructure and Mechanical Properties of Al/Steel Bimetallic Composites Fabricated by Liquid-Solid Casting with Rare Earth Eu Additions. *Materials* **2022**, *15*, 6507. [PubMed]
13. Rajendran, N.; Yurgel, C.C.; Misiolek, W.Z.; Alves de Sousa, R. Hot Forging Die Design Optimization Using FEM Analysis for Near-Net Forming of 18CrNiMo7-6 Steel Pinion Shaft. *Metals* **2023**, *13*, 815.
14. Xu, C.; Cai, X.; Jiao, X.; Vu, K.L.; Shang, Z.; Feng, P. Near-net forming of porous Co-Al by isothermal treatment: Phase formation s equence and diffusion kinetics. *Mater. Charact.* **2023**, *199*, 112785.
15. Bhaskaran Nair, R.; Supekar, R.; Morteza Javid, S.; Wang, W.; Zou, Y.; McDonald, A.; Mostaghimi, J.; Stoyanov, P. High-Entropy Alloy Coatings Deposited by Thermal Spraying: A Review of Strengthening Mechanisms, Performance Assessments and Perspectives on Future Applications. *Metals* **2023**, *13*, 579.
16. Liu, Y.; Wang, Z.; Li, Y.; Yuan, H.; Li, F. The effect of thermal spraying on the forming performance of incremental sheet forming. *J. Mater. Res. Technol.* **2021**, *12*, 776–787.
17. Venkatachalapathy, V.; Katiyar, N.K.; Matthews, A.; Endrino, J.L.; Goel, S. A Guiding Framework for Process Parameter Optimisation of Thermal Spraying. *Coatings* **2023**, *13*, 713.
18. Jalal, Z.; Al-Sultani, K.F.; Majdi, H.S. MWCNTs Addition to Al2O3-SiC Binary Coating Deposited by Plasma Thermal Spray on Low Carbon Steel Substrate. *IOP Conf. Ser. Mater. Sci. Eng.* **2021**, *1094*, 012158.
19. Asmann, M.; Cook, R.F.; Heberlein, J.V.; Pfender, E. Chemical vapor deposition of an aluminum nitride–diamond composite in a triple torch plasma reactor. *J. Mater. Res.* **2001**, *16*, 469–477.
20. Trelles, J.P.; Pfender, E.; Heberlein, J. Multiscale Finite Element Modeling of Arc Dynamics in a DC Plasma Torch. *Plasma Chem. Plasma Process.* **2006**, *26*, 557–575.
21. Goutier, S.; Vardelle, M.; Fauchais, P. Comparison between metallic and ceramic splats: Influence of viscosity and kinetic energy on the particle flattening. *Surf. Coat. Technol.* **2013**, *235*, 657–668. [CrossRef]
22. Xue, S.; Boulos, M. Transient heating and evaporation of metallic particles under plasma conditions. *J. Phys. D Appl. Phys.* **2019**, *52*, 454002. [CrossRef]
23. Dolmaire, A.; Goutier, S.; Vardelle, M.; Geffroy, P.M.; Joulia, A. Investigations on Particle Behavior at the Stagnation Zone for a Suspension Particle Jet in Plasma Spray Conditions. *J. Therm. Spray Technol.* **2021**, *30*, 1001–1014. [CrossRef]
24. Xu, P.; Coyle, T.W.; Pershin, L.; Mostaghimi, J. Fabrication of Superhydrophobic Ceramic Coatings via Solution Precursor Plasma Spray Under Atmospheric and Low-Pressure Conditions. *J. Therm. Spray Technol.* **2019**, *28*, 242–254. [CrossRef]
25. Ivchenko, D.; Mariaux, G.; Vardelle, A.; Goutier, S.; Itina, T.E.; André, P. Feasibility Study of an Adaptive-Pressure Plasma Coating Process—Part 1: Model Description. *J. Therm. Spray Technol.* **2020**, *29*, 25–37.
26. Fikus, B.; Senderowski, C.; Panas, A.J. Modeling of Dynamics and Thermal History of Fe-40Al Intermetallic Powder Particles Under Gas Detonation Spraying Using Propane–Air Mixture. *J. Therm. Spray Technol.* **2019**, *28*, 346–358.
27. Senecal, P.K.; Schmidt, D.P.; Nouar, I.; Rutland, C.J.; Reitz, R.D.; Corradini, M.L. Modeling high-speed viscous liquid sheet atomization. *Int. J. Multiph. Flow* **1999**, *25*, 1073–1097. [CrossRef]
28. Shemyakina, O.A.; Sheikhalieva, Z.I.; Sheikhaliev, S.M. Obtaining Solder Powders by Centrifugal Atomization of Melt. *Russ. J. Non-Ferr. Met.* **2010**, *51*, 250–254. [CrossRef]
29. Gutierrez-Miravete, E.; Lavernia, E.J.; Trapaga, G.M.; Szekely, J.; Grant, N.J. A mathematical model of the spray deposition process. *Metall. Trans. A* **1989**, *20*, 71–85. [CrossRef]

30. Grant, P.S.; Cantor, B.; Katgerman, L. Modelling of droplet dynamic and thermal histories during spray forming—I. Individual droplet behaviour. *Acta Metall. Mater.* **1993**, *41*, 3097–3108.
31. Mathur, P.; Apelian, D.; Lawley, A. Analysis of the spray deposition process. *Acta Metall.* **1989**, *37*, 429–443. [CrossRef]
32. Fu, X.-W.; Zhang, J.-S.; Sun, Z.-Q. Modeling and optimizing software of spray deposition process. *Acta Metall. Sin.* **1999**, *35*, 147–151.
33. Lee, E.S.; Ahn, S. Solidification progress and heat transfer analysis of gas-atomized alloy droplets during spray forming. *Acta Metall. Mater.* **1994**, *42*, 3231–3243. [CrossRef]
34. Ganesan, S.; Poirier, D.R. Solute redistribution in dendritic solidification with diffusion in the solid. *J. Cryst. Growth* **1989**, *97*, 851–859.
35. Wołczyński, W. Development of the jackson and hunt theory for rapid eutectic growth. *Arch. Metall. Mater.* **2018**, *63*, 65–72. [CrossRef] [PubMed]
36. Xie, J.W.; Zhao, Y.Y.; Dunkley, J.J. Effects of processing conditions on powder particle size and morphology in centrifugal atomisation of tin. *Powder Metall.* **2004**, *47*, 168–172.
37. Pijuan, J.; Cegarra, S.A.; Dosta, S.; Albaladejo-Fuentes, V.; Riera, M.D. Centrifugal Atomization of Glass-Forming Alloy Al86Ni8Y4.5La1.5. *Materials* **2022**, *15*, 8159. [CrossRef]
38. Teunou, E.; Poncelet, D. Rotary disc atomisation for microencasulation applications—Prediction of the particle trajectories. *J. Food Eng.* **2004**, *71*, 345–353.
39. Li, H.P. Droplet dynamic and solidification progress duringrotating disk centrifugal atomization. *Trans. Nonferrous Met. Soc. China* **2006**, *16*, 793–799.
40. Mi, J.; Grant, P.S. Modelling the shape and thermal dynamics of Ni superalloy rings during spray forming/Part 2: Thermal modelling-Heat flow and solidification. *Acta Mater.* **2008**, *56*, 1597–1608.

Disclaimer/Publisher's Note: The statements, opinions and data contained in all publications are solely those of the individual author(s) and contributor(s) and not of MDPI and/or the editor(s). MDPI and/or the editor(s) disclaim responsibility for any injury to people or property resulting from any ideas, methods, instructions or products referred to in the content.